ISSN 2712-0554
**Heritage and Sustainable Development** *Original Research*
Vol. 6, No. 1, March 2024, pp.77-90
https://doi.org/10.37868/hsd.v6i1.392

# Effects of selective laser melting process parameters on 3D-printing of Ti6Al4V/ST316L composite material and their optimization using response surface methodology

**Marwa M. Ismaeel[1,2,*], Anwaar A. Al-Dergazly[1], Samah K. AbdulKareem[3], Khider Al-Jaburi[4]**
[1] Department of Laser and Optoelectronics Engineering, Collage of Engineering, Al-Nahrain University, Baghdad, Iraq
[2] Computer Techniques Engineering Department, Baghdad College of Economic Sciences University, Baghdad, Iraq
[3] Al-Turath University College, Baghdad, 10001, Iraq
[4] Department of Aeronautical Technical Engineering, College of Technical Engineering, Al-Farahidi University, Baghdad, Iraq

*Corresponding author: marwa.mustafa1985@gmail.com

Received Jan. 9, 2024
Revised Feb. 22, 2024
Accepted Mar. 3, 2024

**Abstract**

The mechanical properties of Ti6Al4V and ST316L bone implants make them superior to natural bone, which results in fewer contact points with the bone. Different manufacturing processes, such as selective laser melting (SLM), may result in different mechanical properties between Ti-6Al-4V and ST316L implants. Sustainable development for the composite implants was optimized (SLM) in this study to minimize their compressive strength and Young's modulus. A three-dimensional printing process using SLM was optimized based on laser power, hatch distance, laser velocity, and ST316L weight percentage. Composite implants made from titanium alloys and steel alloys were evaluated using response surface methodology (RSM). ST316L composition has been found to influence the mechanical properties of composites in a significant manner, based on the results of parameter optimization. Using Ti6Al4V/ST316L as a biomaterial in knee joint prostheses is possible.



*Keywords*: Sustainable development, Compressive strength, Hatch distance, Laser power, Laser velocity, ST316L, SLM, Ti6Al4V

## 1. Introduction

Production of quality materials with appropriate mechanical properties is one of the practical challenges in orthopedic engineering applications [1]. Ideally, a biomaterial for orthopedic engineering should mimic naturally occurring bone's compressive strength and Young's modulus to distribute loads effectively and reduce stress shielding [2]. Stress shielding reduces the integration of the implant with surrounding bone, thereby causing bone loss and fracture [3]. Most of the currently used biomaterials for orthopedic engineering have Young's modulus higher than bone and stress shielding occurs [4-6]. Metallic biomaterials, e.g. 316L stainless steel, and titanium alloys have been extensively used as bone implant materials. Stainless steel 316L is corrosion corrosion-resistant metallic biomaterial that is easily available and fabricated [7]. The Young's modulus, however, is high. Materials based on titanium, for instance, Ti6Al4V, are becoming increasingly popular for orthopedic applications due to their high biocompatibility, high strength, corrosion resistance, and lower Young's moduli, which are still too high when compared with cortical bone. In contrast to anatomical bone, titanium-based orthopedic implants present higher stiffness and strength, contributing to stress-shielding phenomena that compromise bone integrity. Thus, Young's modulus could be further reduced until it is more

like human bone [8-11]. Additive manufacturing (AM) also known as 3D-printing is a manufacturing process in which each part is formed layer by layer in a controlled manner using computer-aided software. One technique of AM, selective laser melting (SLM), is widely used for fabricating high-strength alloys for biomedical applications [12, 13]. Laser power, scanning speed, metal powder layer thickness, printer precision, and other printing conditions are all known to affect the physical and mechanical characteristics of final printed products [14, 15]. The purpose of this study was to investigate the effectiveness of SLM parameters like laser power, hatch distance, laser velocity, and ST316L weight percentage on compression strength and Young's modulus of composite alloys processed using SLM. Using the RSM, we determined the best conditions for the SLM process parameters to reduce Ti6Al4V/ST316L compressive strength and achieve human bone-like Young's modulus.

## 2. Methods

### 2.1. Experimental design

The SLM 3D-printing process of Ti6Al4V/ST316L composite implants was developed using a Faced Center RSM experimental design using Design-Expert 11.0, and three levels of SLM process parameters were evaluated. On the Young's modulus and compressive strength of Ti6Al4V/ST316L composite implants with laser power of 80, 90, and 100 W; hatch distances of 0.08, 0.11, and 0.14 mm; laser speeds of 100, 300, and 500 mm/s; and ST316L contents of 0, 25, and 50 wt% (Table 1).

Table 1. SLM process parameters

| Variable | Unit | Notation | Level |
|---|---|---|---|
| Laser power | W | A | 80, 90, 100 |
| Hatch distance | mm | B | 0.08, 0.11, 0.14 |
| Laser velocity | mm/s | C | 100, 300, 500 |
| ST316L composition | wt% | D | 0, 25, 50 |

The software suggested thirty runs for implant fabrication (Table 2). The proper relation between the parameters can be obtained by analyzing the responses of these thirty runs. The statistical significance of the model was measured by determining the P-values. A P-value less than 0.05 represents the significance of the factor on the response.

Table 2. Based on the experimental values of Young's modulus and compressive strength of the materials are experimentally measured in the SLM 3D printing process

| Trial No. | Levels | | | | R1: Young modulus (MPa) | R2: Compressive strength (MPa) |
|---|---|---|---|---|---|---|
| | A | B | C | D | | |
| 1 | 90 | 0.11 | 300 | 25 | 4356.12 | 357.3 |
| 2 | 90 | 0.11 | 300 | 25 | 4282.02 | 358.5 |
| 3 | 90 | 0.11 | 300 | 25 | 4316.37 | 357.5 |
| 4 | 90 | 0.11 | 300 | 25 | 4306.12 | 358.6 |
| 5 | 90 | 0.11 | 300 | 25 | 4396.39 | 353.8 |
| 6 | 90 | 0.11 | 300 | 25 | 4296.42 | 354.7 |
| 7 | 90 | 0.11 | 300 | 50 | 912.58 | 74.4 |
| 8 | 90 | 0.11 | 300 | 0 | 2904 | 496 |
| 9 | 90 | 0.11 | 500 | 25 | 5394 | 351.8 |
| 10 | 90 | 0.11 | 100 | 25 | 5463 | 352.8 |
| 11 | 90 | 0.14 | 300 | 25 | 3887 | 248 |
| 12 | 90 | 0.08 | 300 | 25 | 3508 | 357 |
| 13 | 100 | 0.11 | 300 | 25 | 3899 | 376 |
| 14 | 80 | 0.11 | 300 | 25 | 4432.07 | 438 |

| Trial No. | Levels | | | | R1: Young modulus (MPa) | R2: Compressive strength (MPa) |
|---|---|---|---|---|---|---|
| | A | B | C | D | | |
| 15 | 100 | 0.14 | 500 | 50 | 1377.95 | 59.7 |
| 16 | 80 | 0.14 | 500 | 50 | 817.45 | 40.5 |
| 17 | 100 | 0.08 | 500 | 50 | 1563.83 | 106 |
| 18 | 80 | 0.08 | 500 | 50 | 1125.58 | 103 |
| 19 | 100 | 0.14 | 100 | 50 | 933 | 84.7 |
| 20 | 80 | 0.14 | 100 | 50 | 698.37 | 78.9 |
| 21 | 100 | 0.08 | 100 | 50 | 870 | 109 |
| 22 | 80 | 0.08 | 100 | 50 | 1070 | 155 |
| 23 | 100 | 0.14 | 500 | 0 | 2420 | 398 |
| 24 | 80 | 0.14 | 500 | 0 | 3114.5 | 482.6 |
| 25 | 100 | 0.08 | 500 | 0 | 1997 | 558.4 |
| 26 | 80 | 0.08 | 500 | 0 | 2870.97 | 658 |
| 27 | 100 | 0.14 | 100 | 0 | 3044 | 344.7 |
| 28 | 80 | 0.14 | 100 | 0 | 3962.26 | 451 |
| 29 | 100 | 0.08 | 100 | 0 | 2244.3 | 482 |
| 30 | 80 | 0.08 | 100 | 0 | 3868 | 641.6 |

The considered responses including R1: Young's modulus (MPa), and R2: Compressive strength (MPa) were measured, and the data was analyzed by the software. The relation between SLM 3D-printing process parameters was demonstrated by a mathematical equation (Equations 1 and 2). The effect of SLM 3D-printing process parameters on Young's modulus and compressive strength are presented in Table 3.

### 2.2. Process parameters optimization

The parameters for SLM 3D printing, i.e. laser power, hatch distance, laser velocity, and ST316L wt% were optimized to manufacture proper implants for orthopedic applications. For the claimed application, the suitable range of Young's modulus for human bone is 0.05-0.5 GPa for trabecular bone and 7-30 GPa for cortical bone, and the range of compressive strength for human bone is 0.16-20 MPa for trabecular bone and 130-200 MPa for cortical bone [16]. For optimization of process parameters, Young's modulus was set to its range value, and the compressive strength was set to a range of 130-200 MPa. The optimization was done by software. The optimum Ti6Al4V/ST316L composite implant was 3D printed in an optimum condition of the parameters.

### 2.3. Mechanical properties

Using a computerized universal testing machine (Zwick Tehran, Iran) with a 5-tone load cell, static compression loading was conducted at ambient temperature (25oC) using a unidirectional vertical piston. Figure 1 shows the implants being compressed until failure. With the help of stress-strain curves, Young's modulus and compressive strength values were determined. A triplicate test was conducted on each implant.

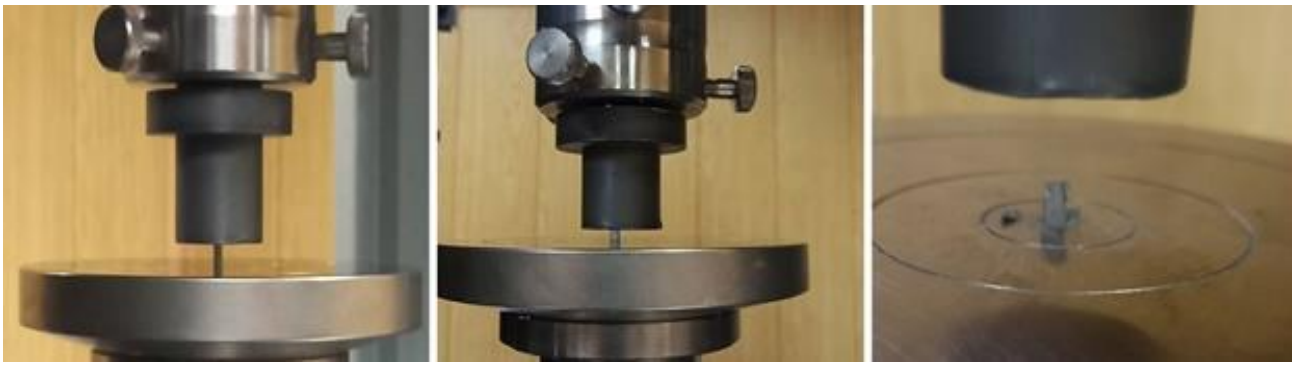

Figure 1. Compression of SLM-processed Ti6Al4V/ST316L implant

### 2.4. Characterization of the optimized Ti6Al4V/ST316L composite implant

#### 2.4.1. Elemental composition

Ti6Al4V/ST316L composite implants processed by SLM were analyzed using elemental maps analyzed using energy dispersive spectroscopy (EDS) by Zeiss, Oberkochen, Germany.

#### 2.4.2. X-ray diffraction analysis

This experiment was conducted using an X-ray diffractometer (PW1730, Philips, Amsterdam, The Netherlands). There were 0.05 o steps, 1 second time steps, 40 kV voltage, and 30 mA current steps, respectively.

#### 2.4.3. Surface topography and morphology

Scanning electron microscopy (SEM; Zeiss, Oberkochen, Germany) was used to observe the surface topography and morphology of SLM processed Ti6Al4V/ST316L implant using gold coating. The optimum electron accelerating voltage and working distance were 15 kV, and 10 mm respectively.

#### 2.4.4. Surface wettability

Surface hydrophilicity of SLM processed pure Ti6Al4V and Ti6Al4V/ST316L composite implant was evaluated using water contact angle measurement. A video contact angle system (Sony color video camera, Tokyo, Japan) was used to capture the water contact angle image on the surface of pure Ti6Al4V and Ti6Al4V/ST316L composite implants. The measurement was repeated with three samples.

#### 2.4.5. In vitro biocompatibility

MC3T3-E1 pre-osteoblasts (American Type Culture Collection, Manassas, VA, USA) were used to evaluate cell proliferation and viability on SLM-processed pure Ti6Al4V and Ti6Al4V/ST316L implants. The cells were used at third to fourth passage for experiments. Before cell seeding, the implants were sterilized with UV for 30 min, and 70% ethanol for 1 h. 50 microliters of cell suspension in α-Minimum Essential medium (α-MEM) containing 10% fetal bovine serum (FBS) were seeded onto the implants in a 24-well plate and kept in 5% $CO_2$ in air at 37°C for seven days. AlamarBlue® fluorescent assay was used to evaluate MC3T3-E1 cell proliferation at days 1, 3, and 7, and cell viability after 1 day on SLM-processed pure Ti6Al4V and Ti6Al4V/ST316L composite implants. At days 1, 3, and 7, 10% AlamarBlue® in culture medium was added to the wells and incubated 5% $CO_2$ in air at 37°C for 4 h. The fluorescence was measured at 530 nm. Optical density (OD) was used to perform cell proliferation rate. OD values normalized to the relative value of the control (cell culture plate) on day 1 were used to analysis of the cytotoxicity.

#### 2.4.6. In vivo biocompatibility

In vivo, the biocompatibility of the implants was evaluated by implantation in rabbit femur. Twelve rabbits with an approximate weight of 2.5 kg were used in this study. The implants were sterilized by autoclave at 121 °C for 20 min. The rabbits were cared for in compliance with an approved protocol from the Institutional Animal Care Committee. The rabbits were anesthetized using ketamine (10 mg/kg) and midazolam (0.1 mg/kg). The right leg of the rabbit was cleaned with iodine and shaved. The femoral proximal-cranial section was cut which penetrated all soft tissue layers. Holes were made using a drill. The implant was inserted inside the hole using finger pressure (Figure 2). After implantation is done, the implant sites are sutured. Meloxicam was given to each rabbit every 3 days to reduce pain and inflammation. Animals were followed for 6 weeks by providing food and water. At the end of 6 weeks, an intracardiac injection of 10 mg/kg ketamine was used to sedate the animals. The implanted femoral site was removed for further analysis.

#### 2.4.7. Eosin and hematoxylin staining

To visualize the femoral implant site, hematoxylin and eosin were stained. Formaldehyde was used to fix bone samples for H&E staining. The fixed bone sampled was completely decalcified with EDTA solution. The

paraffin blocks were made and 5 µm sections were stained H&E. Optical images were taken under a light microscope (Nikon TE2000-U; Nikon Corporation).

### 2.5. Modeling based on finite elements

#### 2.5.1. Model designs

The geometrical model of the implants and bones was realized with CATIA software using magnetic resonance images (MRI). The models were imported into Abacus software for FE modeling. It was assumed both tibia and femur inserts were completely osteointegrated and bonded to the tibia and femur bones.

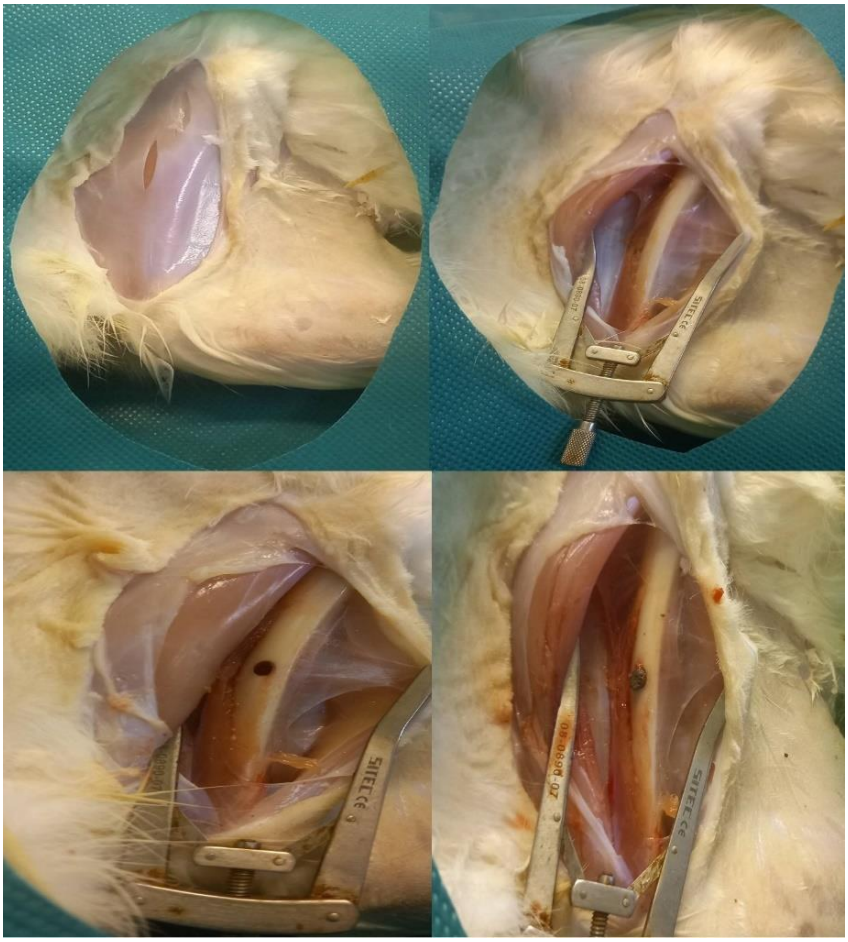

Figure 2. Animal surgical and implantation

#### 2.5.2. Boundary conditions

The femur section applied a static compressive load of F y = 2667 N in the 'y' direction. Tibia bones were fixed at their apex, allowing rotation around the X, Y, and Z axes.

#### 2.5.3. Finite-element mesh

In Hypermesh v14.0 software (Altair Engineering, Troy, MI, United States), triangular structures were generated on all components. There was zero displacement enforced between the femur and tibia bones and inserts since they were frozen contacts. A sensitivity study was conducted to ensure high-quality results. We conducted a mesh convergence study using adaptive elements (0.8 to 2mm in size) to get accurate numerical results.

#### 2.5.4. Material properties

Analyses were performed on the femur and tibia bone ends. It was assumed that femurs and tibias had homogeneous and isotropic properties.

## 3. Results

### 3.1. The effect of designed parameters on the mechanical properties

The effect of SLM 3D-printing process parameters i.e. power (A), hatching space (B), printing speed (C), and ST316L wt% (D) on mechanical properties are shown in Table 3 and Figures 3, 4, and 5. According to the results, a quadratic relation between significant factors ($p < 0.05$) is suggested by the software.

Table 3. An analysis of variance (ANOVA) for fitting a quadratic response surface model

| Source | P-value | |
|---|---|---|
| | Young modulus (MPa) | Compressive strength (MPa) |
| Model | Less than 0.0001 | Less than 0.0001 |
| A-Laser power | Less than 0.0001 | Less than 0.0001 |
| B-Hatch distance | 0.0162 | Less than 0.0001 |
| C-Laser velocity | 0.0032 | 0.0462 |
| D-ST316L composition | Less than 0.0001 | Less than 0.0001 |
| AB | 0.0024 | Less than 0.0001 |
| AC | 0.0002 | Less than 0.0001 |
| AD | Less than 0.0001 | Less than 0.0001 |
| BC | 0.3135 | 0.5290 |
| BD | Less than 0.0001 | Less than 0.0001 |
| CD | Less than 0.0001 | Less than 0.0001 |
| $A^2$ | 0.0026 | Less than 0.0001 |
| $B^2$ | Less than 0.0001 | Less than 0.0001 |
| $C^2$ | Less than 0.0001 | 0.7151 |
| $D^2$ | Less than 0.0001 | Less than 0.0001 |

According to Figure 3, the compressive strength has increased as laser power, hatch distance, and ST316L composition decreased especially at a lower value of ST316L composition. The terms A, B, C, D, AB, AC, AD, BD, CD, $A^2$, $B^2$, and $D^2$ are significant model terms ($p < 0.05$).

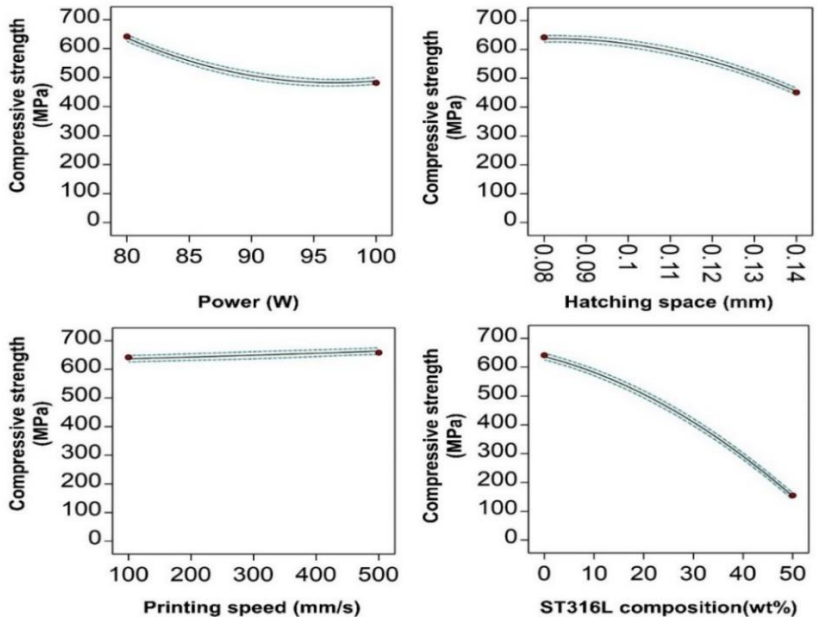


Figure 3. Effect of SLM 3D-printing power, hatching space, printing speed, and ST316L composition on Compressive strength of Ti6Al4V/ST316L implants

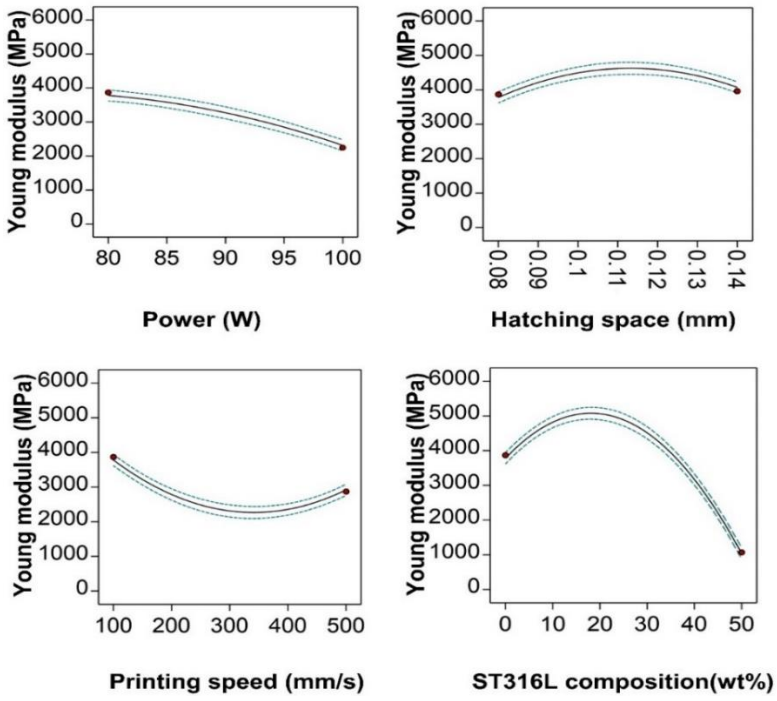


Figure 4. Effect of SLM 3D-printing power, hatching space, printing speed, and ST316L composition on Young modulus of Ti6Al4V/ST316L implants

According to Figure 5, the interaction effect of laser power and hatch distance on Young's modulus indicates that the maximum Young's modulus occurs in the laser power between 80-85W and hatch distance of 0.1-0.125 mm. The interaction effect of laser power and laser velocity on Young's modulus indicates that the increase or decrease in the laser velocity has no strong effect on the young modulus. The contour plot of interaction effects of ST316L composition and laser power indicates that the maximum Young's modulus occurs in the ST316L composition of 15-25 wt%. According to Figure 3, the increase in laser power and hatch distance decreases the compressive strength. The increase in laser velocity has slightly increased the compressive strength. ST316L composition has a strong effect on compressive strength. The increase in ST316L composition from 0 to 50 wt%, decreased the compressive strength from 600 to 100 MPa. The compressive strength of 250 MPa which is the cortical bone compressive strength occurred at ST316L composition of >25 wt%.

According to contour plots of the interaction effects between the hatch distance-laser power, laser velocity-laser power, ST316L composition-laser power, ST316L composition-hatch distance, and ST316L composition-laser velocity, the target compressive strength of 250 MPa, which is the compressive strength of cortical bone occurs in the laser power of 80-100 W, the laser velocity of 100-500 mm/s, the hatch distance of 0.08-0.14 mm and the ST316L composition of 40-50 wt%. These results indicate that the ST316L composition (wt%) has the strongest effect on compressive strength and is a dominant parameter. A response surface model of significant factors ($p < 0.05$) is obtained as below:

$$\text{Young's modulus (MPa)} = -13018.8 + 292.661A + 149481B - 22.2884C + 51.0955D + 300.373AB + 0.0605503AC + 1.28595AD - 196.928BD + 0.0503691\ CD - 2.2004A^2 - 764528B^2 + 0.0260731\ C^2 - 3.96366\ D^2 \quad (1)$$

$$\text{Compresive strength (MPa)} = +353.136 - 29.45A - 54.55B + 3.23889C - 205.617D + 8.51875AB + 9.00625AC + 27.0062AD + 28.4062BD - 18.5063CD + 56.1614A^2 - 48.3386B^2 - 65.6386\ D^2 \quad (2)$$

Among the coded variables are A, B, C, and D, which correspond to laser power, hatch distance, laser velocity, and ST316L weight percent. As shown in Figure 6, the model's predicted values are in good agreement with experimental values.

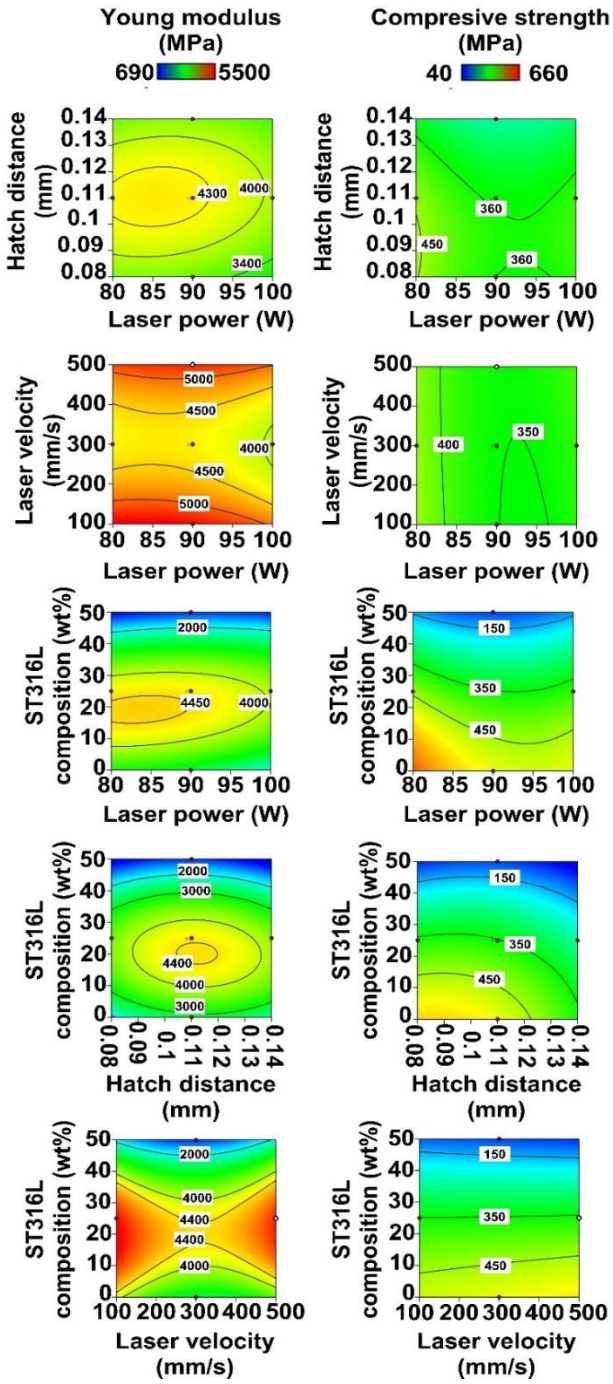


Figure 5. Interaction effect of SLM 3D-printing power, hatching space, printing speed, and ST316L composition on Young's modulus and compressive strength of Ti6Al4V/ST316L implants

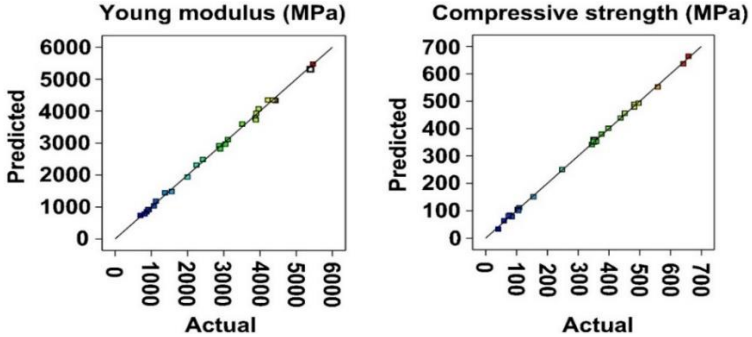


Figure 6. The experimental and predicted response of Young's modulus and compressive strength

### 3.2. Optimized process parameters

The optimized values for SLM 3D-printing process parameters, *i.e.* laser power, hatch distance, laser velocity, and ST316L wt%, and predicted results for Young's modulus and compressive strength were achieved as presented in Table 4.

Table 4. Optimized SLM 3D-printing process parameters

| Laser power | Hatch distance | Laser velocity | ST316L wt% | Young's modulus | Compressive strength | Desirability |
|---|---|---|---|---|---|---|
| 80.000 | 0.08 | 100.000 | 50.000 | 1034.384 | 151.526 | 1.000 |

### 3.3. Mechanical properties

To determine the magnitude of von Mises stress in regions of high compression strain in the implant, we measured the von Mises stress magnitude and distribution in the bone and implant. The implant would likely fail if the von Mises stress values exceeded the material's compression yield strength value. According to Figure 5, the implant is near the failure threshold when the von Mises stress distribution is done. Both Figure 7 (A and B) demonstrate similar stress distributions between the implants. Implants showed homogeneous von Mises stress distributions. Maximum von Mises stress ranged between 10.82-19.5 MPa. In all implants, the von Mises stress was not greater than the yield stress of the bulk material.

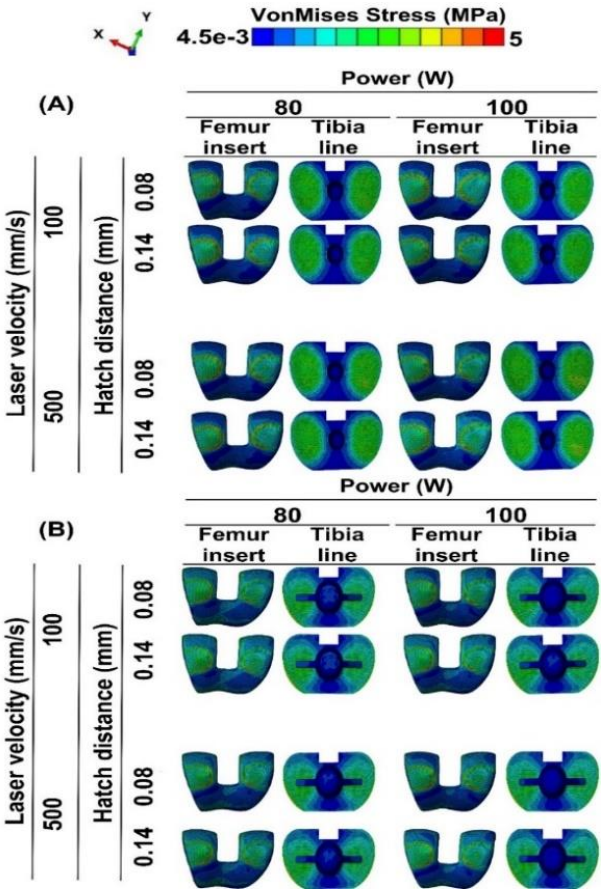


Figure 7. Von Mises stress distribution and magnitude on femoral and tibial insert of the implants at ST316L composition of (A) 50 wt%, and (B) 0 wt%

### 3.4. Elemental composition

According to the EDS micrograph (Figure 8), elemental composition reveals the existence of Ti6Al4V and ST316L in the implant which is homogeneously dispersed in the implant structure [17, 18]. The content of each component in the structure is C: 20.94%, O: 10.45%, Al: 3.69%, Si: 0.36%, Ti: 44.89%, V: 2.26%, Cr: 3.41%, Fe: 12.11%, and Ni: 1.89%.

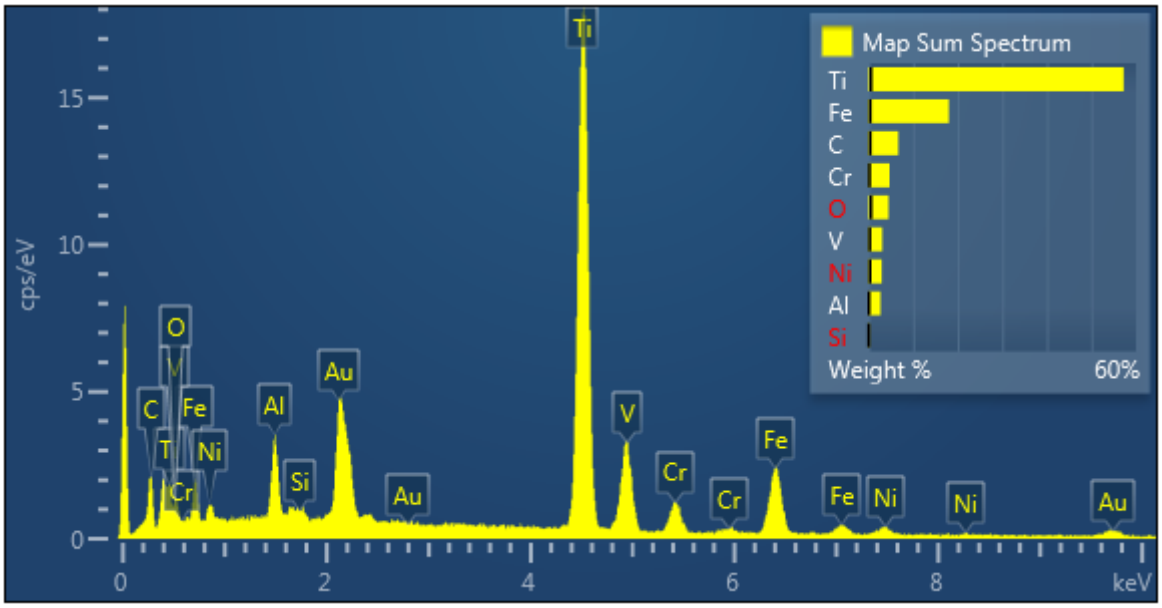


Figure 8. EDC micrograph of Ti6Al4V implant

### 3.5. Surface topography

Image of implant surface topography taken with a scanning electron microscope. Figure 7 shows irregularities on the surface with small peaks and troughs. The microscale roughness of our implant surface affected protein adsorption and cell behavior. Cell attachment, viability, and osteogenic differentiation are improved by surface roughness at a micron scale [19, 20]. Microns are the unit of measurement for the roughness distribution on the implant surface. It has been demonstrated for titanium with an increased surface roughness that these implants promote cell attachment and viability in vitro [21]. Adsorption of proteins from body fluids influences cell attachment and behavior, e.g. osteogenic differentiation and proliferation. An increase in surface roughness promotes protein adsorption and enhances cell function [22].

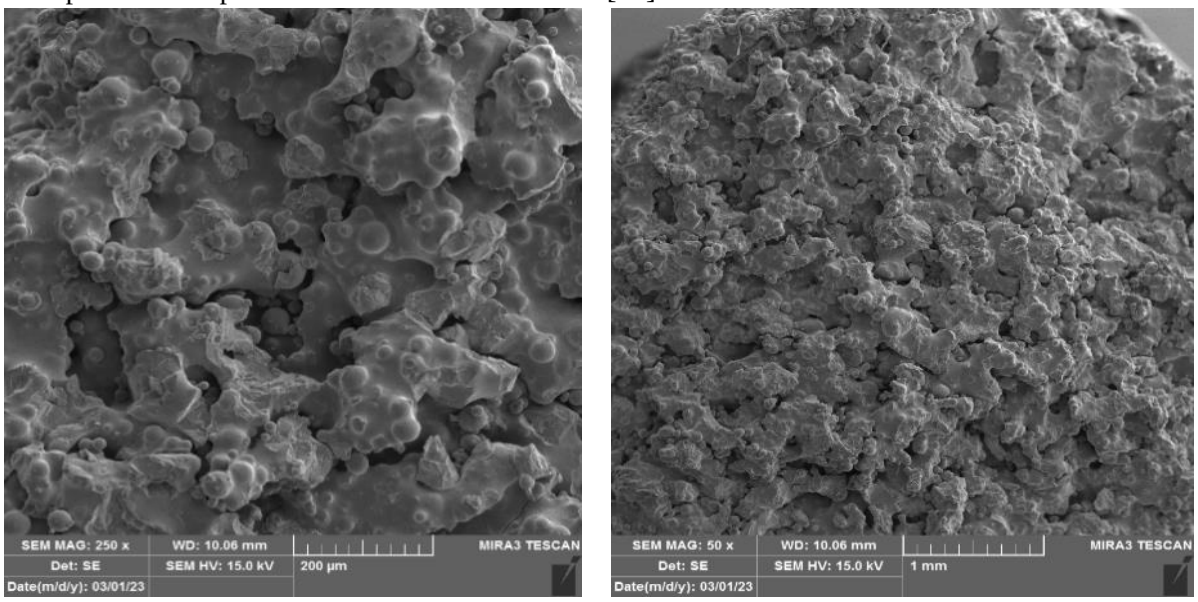


Figure 9. SEM images of the Ti6Al4V/ST316L implant

### 3.6. Phase identification with XRD micrograph

The X-ray powder diffraction (XRD) analytical technique was used to determine the phase of the SLM Ti6Al4V/ST316L, Ti6Al4V powder, and ST316L powder (Figure 10). Ti6Al4V XRD diffraction peaks were detected at 40°, which indicates Ti6Al4V has a structure consistent with the peaks. Further, the peaks at 53° correspond to the structure of ST316L [23, 24].

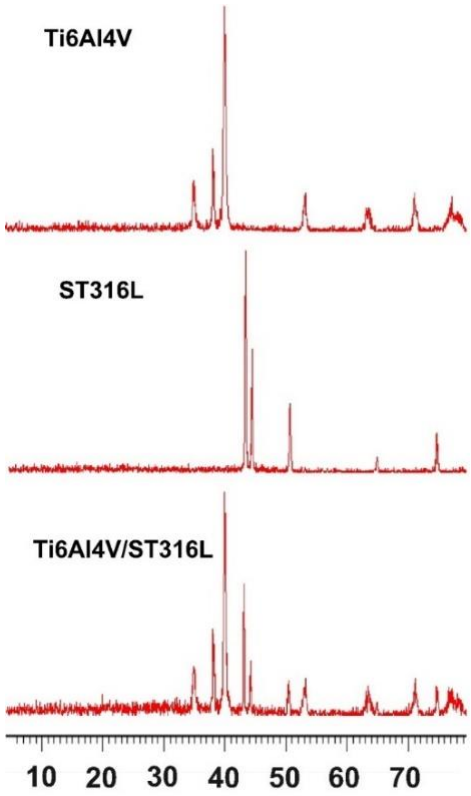


Figure 10. XRD micrograph of Ti6Al4V, ST316L, and Ti6Al4V/ST316L implant

### 3.7. Surface wettability

The surface wettability of SLM 3D-printed Ti6Al4V and Ti6Al4V/ST316L composite implants were analyzed by water contact angle measurement (Figure 11). The water contact angle of the SLM 3D-printed Ti6Al4V implant was 85.7±2.9°. The water contact angle of the SLM 3D-printed Ti6Al4V/ST316L composite decreased to 61.1±2.2°. The decrease (0.72-fold, $p<0.0005$) in water contact angle of SLM 3D-printed Ti6Al4V/ST316L composite implant compared to SLM 3D-printed Ti6Al4V implant will increase protein adsorption and enhance cell interaction with the implant's surface resulting increased osteointegration of SLM 3D-printed Ti6Al4V/ST316L composite implant [21].

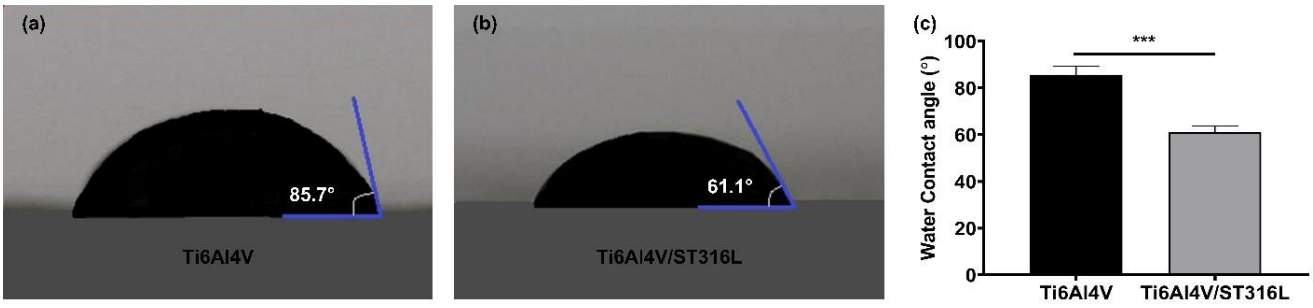


Figure 11. Wettability of the Ti6Al4V implant

### 3.8. In vitro biocompatibility

MC3T3-E1 preosteoblasts proliferation was increased (1.07-fold, $p<0.05$, day 1; 1.03-fold, $p<0.005$, day 3; 1.2-fold, $p<0.05$, day 7) on Ti6Al4V/ST316L composite implant compared to Ti6Al4V implants (Figure 12). Cell viability was 91.7±0.6% on Ti6Al4V implants. The cell viability increased to 97.6±0.1.8% on Ti6Al4V/ST316L implants (Figure 12). The increase in cell proliferation and cell viability on Ti6Al4V/ST316L implants

compared to Ti6Al4V implants is due to increased surface wettability. Protein adsorbs to the surface before cell attachment. The protein adsorption controls cell attachment and behavior. Surface wettability enhances protein adsorption, hence increases cell attachment, proliferation, and cell viability, which is in good agreement with our results [21].

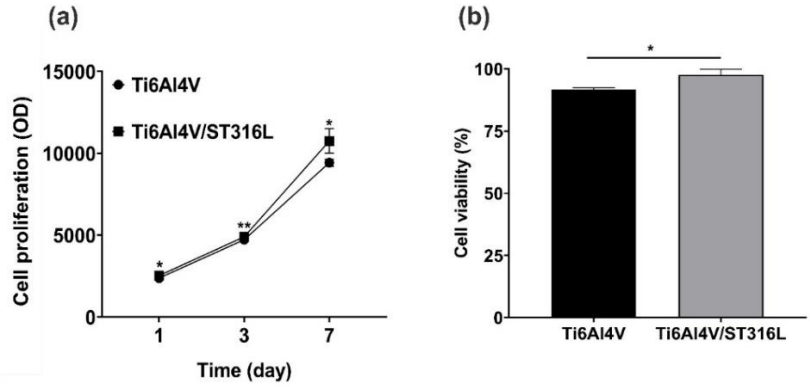


Figure 12. Cell proliferation on optimized Ti6Al4V/ST316L implants

### 3.9. In vivo biocompatibility

After 6 weeks of implantation of Ti6Al4V and Ti6Al4V/ST316L implants in the rabbit femur, the local bone tissue at the implanted sites was harvested and analyzed by H&E staining (Figure 13). According to H&E stained images, there was no cell necrosis, and the cell membrane and nuclei were intact. The inflammatory cell infiltration was not detected in the implanted site tissue. Degradation and osteolysis of bone were not found. Osteoblasts, osteocytes, and blood vessels are in normal structure. The sectioned bone is in the normal bone and no pathologic changes were seen.

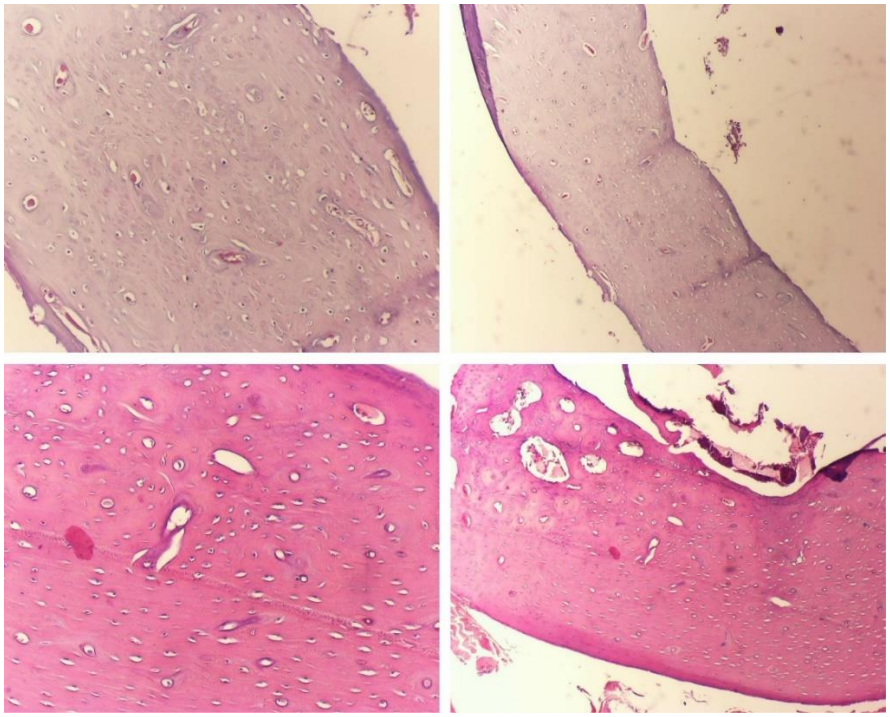

Figure 13. H&E analysis of rabbit femur bone implanted with optimized Ti6Al4V/ST316L implant

## 4. Conclusions

In this work, selective laser melting parameters, i.e. power, hatching, speed, and ST316L composition in 3D-printing of Ti6Al4V knee implants were optimized using response surface methodology. Studying the effect of printing parameters and ST316L composition on the mechanical properties of Ti6Al4V/ST316L composites

revealed that ST316L composition has the strongest effect on the mechanical properties of the composite. SLM 3D printed Ti6AL4V/ST316L composite with the composition of 50/50 has appropriate mechanical properties in comparison to the human bone, which can be a better candidate as biomaterials for orthopedic implants.

**Declaration of competing interest**

The authors declare that they have no known financial or non-financial competing interests in any material discussed in this paper.

**Funding information**

No funding was received from any financial organization to conduct this research.

**Ethical approval statement**

Ethical approval for reporting this case was obtained from Al-Nahrain University, College of Engineering (1178/2/1, 2022/7/25).

**Informed consent**

Informed consent was obtained from the owner of the animals prior to their participation in the research study.

**References**

[1] L. C. Campanelli, "A review on the recent advances concerning the fatigue performance of titanium alloys for orthopedic applications," *J. Mater. Res.*, vol. 36, no. 1, pp. 151–165, 2021.
[2] D. M. Robertson, L. Pierre, and R. Chahal, "Preliminary observations of bone ingrowth into porous materials," *J. Biomed. Mater. Res.*, vol. 10, no. 3, pp. 335–344, 1976.
[3] H. J. Rack and J. I. Qazi, "Titanium alloys for biomedical applications," *Mater. Sci. Eng. C Mater. Biol. Appl.*, vol. 26, no. 8, pp. 1269–1277, 2006.
[4] M. Navarro, A. Michiardi, O. Castaño, and J. A. Planell, "Biomaterials in orthopaedics," *J. R. Soc. Interface*, vol. 5, no. 27, pp. 1137–1158, 2008.
[5] Q. Chen and G. A. Thouas, "Metallic implant biomaterials," *Mater. Sci. Eng. R Rep.*, vol. 87, pp. 1–57, 2015.
[6] M. Niinomi, M. Nakai, and J. Hieda, "Development of new metallic alloys for biomedical applications," *Acta Biomater.*, vol. 8, no. 11, pp. 3888–3903, 2012.
[7] M. Semlitsch and H. G. Willert, "Properties of implant alloys for artificial hip joints," *Medical and Biological Engineering and Computing*, vol. 18, pp. 511–520, 1980.
[8] E. Nyberg, M. Miller, K. Simmons, and K. S. Weil, "Microstructure and mechanical properties of titanium components fabricated by a new powder injection molding technique," *Mater. Sci. Eng. C Mater. Biol. Appl.*, vol. 25, no. 3, pp. 336–342, 2005.
[9] E. Nyberg, M. Miller, K. Simmons, and K. S. Weil, "Microstructure and mechanical properties of titanium components fabricated by a new powder injection molding technique," *Mater. Sci. Eng. C Mater. Biol. Appl.*, vol. 25, no. 3, pp. 336–342, 2005.
[10] Kodama T., "Study on biocompatibility of titanium alloys," *Kokubyo Gakkai Zasshi*, vol. 56, no. 2, pp. 263–288, 1989.
[11] M. Kaya and F. Yakuphanoğlu, "A study on microstructure of porous TiNbZr alloy produced as biomaterial," *Materwiss. Werksttech.*, vol. 50, no. 6, pp. 742–746, 2019.
[12] F. I. Hussein Al-Najjar, "Numerical analysis of the effect of scanning speed on the temperature field distribution for laser heat treatment applications," *Al-Nahrain Journal of Engineering Science*, vol. 21, no. 2, pp. 213–222, 2018.
[13] S. Kumawat, S. R. Deshmukh, and R. R. Ghorpade, "Fabrication of Ti-6Al-4v cellular lattice structure using selective laser melting for orthopedic use: A review," in *Materials Today: Proceedings*, 2023.
[14] D.S. Shim, "Effects of process parameters on additive manufacturing of aluminum porous materials and their optimization using response surface method," *J. Mater. Res. Technol.*, vol. 15, pp. 119–134, 2021.

[15] S. A. Naghavi *et al.*, "A novel hybrid design and modelling of a customised graded Ti-6Al-4V porous hip implant to reduce stress-shielding: An experimental and numerical analysis," *Front. Bioeng. Biotechnol.*, vol. 11, p. 1092361, 2023.
[16] L.-C. Gerhardt and A. R. Boccaccini, "Bioactive glass and glass-ceramic scaffolds for bone tissue engineering," *Materials (Basel)*, vol. 3, no. 7, pp. 3867–3910, 2010.
[17] A. Moosa, M. K. Abbas, and R. Mohammed, "Improving Oxidation Resistance of Stainless Steel (AISI 316L) by Pack Cementation," *Engineering and Technology Journal*, vol. 25, no. 7, 2007.
[18] X.-Z. Lin, M.-H. Zhu, J.-F. Zheng, J. Luo, and J.-L. Mo, "Fretting wear of micro-arc oxidation coating prepared on Ti6Al4V alloy," *Trans. Nonferrous Met. Soc. China*, vol. 20, no. 4, pp. 537–546, 2010.
[19] H. Zhang, J. Han, Y. Sun, Y. Huang, and M. Zhou, "MC3T3-E1 cell response to stainless steel 316L with different surface treatments," *Mater. Sci. Eng. C Mater. Biol. Appl.*, vol. 56, pp. 22–29, 2015.
[20] M. Lukaszewska-Kuska, P. Wirstlein, R. Majchrowski, and B. Dorocka-Bobkowska, "Osteoblastic cell behaviour on modified titanium surfaces," *Micron*, vol. 105, pp. 55–63, 2018.
[21] T. Akkas, "Which is more effective for protein adsorption: surface roughness, surface wettability or swelling? Case study of polyurethane films prepared from castor oil and poly (ethylene glycol)," *Polymer International*, vol. 62, no. 8, pp. 1202–1209, 2013.
[22] S. Kim, H.-B. Pyo, S. H. Ko, C. S. Ah, A. Kim, and W.-J. Kim, "Fabrication of anionic sulfate-functionalized nanoparticles as an immunosensor by protein immobilization," *Langmuir*, vol. 26, no. 10, pp. 7355–7364, 2010.
[23] B. Wu *et al.*, "Effects of synchronized magnetic arc oscillation on microstructure, texture, grain boundary and mechanical properties of wire arc additively manufactured Ti6Al4V alloy," *Addit. Manuf.*, vol. 54, no. 102723, p. 102723, 2022.
[24] P. Nath, D. Nanda, G. P. Dinda, and I. Sen, "Assessment of microstructural evolution and mechanical properties of laser metal deposited 316L stainless steel," *J. Mater. Eng. Perform.*, vol. 30, no. 9, pp. 6996–7006, 2021.